

Dual-bell nozzle with fluidic control of transition for space launchers

Andrea Ferrero^{a,*}, Antonietta Conte^a, Emanuele Martelli^b, Francesco Nasuti^c, Dario Pastrone^a

^a*Department of Mechanical and Aerospace Engineering, Politecnico di Torino, Corso Duca degli Abruzzi 24, Turin, 10129, Italy*

^b*Department of Engineering, Università degli Studi della Campania Luigi Vanvitelli, Via Roma 29, Aversa, 81031, Italy*

^c*Department of Mechanical and Aerospace Engineering, Sapienza Università di Roma, Via Eudossiana 18, Rome, 00184, Italy*

Abstract

The dual-bell nozzle is a promising concept for improving the performance of space launchers. It is characterised by the presence of two altitude-dependent working modes which allow to reduce non-adaptation losses. However, the transition between the two working modes usually takes place prematurely and dangerous side loads might be observed. In this work, fluidic control is investigated as a potential method to delay the transition and limit the risk of side loads. An Ariane 5-like launcher configuration with a dual-bell nozzle in the core engine is considered. First, a parametric optimisation is performed to identify the dual-bell geometry that maximises the payload mass delivered into geostationary transfer: a preliminary model is adopted to describe the dual-bell mode transition and a fast and reliable in-house trajectory optimisation code is used to optimise the ascent trajectory. The flow field in the optimal geometry is then investigated by CFD simulations to verify the effectiveness of fluidic control. Finally, the CFD study results are used to model the dual-bell mode transition and trajectory optimisation is performed again. The proposed solution is characterised by a large payload gain with respect to the reference launcher. Fluidic control significantly reduces side loads which can arise during transition.

*Corresponding author

Email address: andrea_ferrero@polito.it (Andrea Ferrero)

Keywords: Dual-bell nozzle, Side loads, Fluidic control, Trajectory optimisation

1. Introduction

Rocket engines used in the first stage of space launchers work from sea-level to almost vacuum conditions. An example is represented by the Vulcain 2 liquid rocket engine used in the Ariane 5 launcher. The area ratio of its nozzle is limited by the necessity to avoid uncontrolled separation and dangerous side loads at lift-off. This limitation has a significant impact on the engine's performance when high altitudes are reached.

In order to avoid such limitations of classical bell nozzles, several alternatives have been proposed and studied [1]: nozzles with fixed insert [2], nozzles with temporary insert [3], Expansion-Deflection nozzles [1], nozzles with forced gas injection [4], plug nozzles [5], dual-bell nozzles [6–11], vented nozzles [12], nozzles with separation avoiding devices [13, 14], nozzles controlled by plasma actuators [15] and nozzle with gas injection [16]. Among them, the dual-bell nozzle represents a promising solution because of its effectiveness and the minor changes it requires with respect to conventional nozzles. The basic idea is to consider a bell shaped nozzle connected to a bell shaped extension by means of an inflection: the discontinuity in the contour slope allows anchoring the separation line and avoiding side loads at low altitudes. When the external pressure reduces below a threshold value, transition occurs and full flow working conditions are obtained. The presence of these two working modes significantly improves the specific impulse, which strongly affects launcher performance especially at higher altitudes where actual payload mass fraction is larger. However, two drawbacks related to the transition process have been individuated during the various feasibility studies. The first one is associated to an early transition to the high-altitude working mode which would limit the performance gain [8]. The second one is far more critical as it is a possible obstacle to the real implementation of this solution: significant side loads can be observed during the transition process [17, 18]. Several strategies have been investigated to control the transition, such as fluidic control [19–21], film cooling [22–25], and mixture ratio variation [25]. Fluidic control is a promising strategy which consists in injecting fluid through a slot near the inflection point; the injected fluid represents an obstacle to the supersonic flow and allows control of the separation line.

34 In this work, a configuration inspired by the Ariane 5 launcher with a
35 dual-bell in the core engine is studied, and fluidic control is investigated as
36 a potential strategy to delay the transition and limit the magnitude of side
37 loads. First of all, a preliminary optimisation study is performed on the
38 dual-bell geometry and on the launcher trajectory to maximise the payload
39 gain. This preliminary optimisation is based on the assumption that fluidic
40 control is able to increase the transitional nozzle pressure ratio (NPR) to the
41 optimal value corresponding to the best performance.

42 As a second step, the flow field inside the optimal dual-bell nozzle is in-
43 vestigated by CFD simulations for several values of NPR to verify the fluidic
44 control effectiveness. The CFD study enabled the determination in more
45 detail of the fluidic control requirements in terms of mass flow rate and ac-
46 tivation time. These data are then used to update the optimal solution.

47

48 **2. Preliminary optimisation for dual-bell geometry selection**

49 A coupled trajectory/nozzle optimization is carried out to identify a suit-
50 able dual-bell geometry. An Ariane 5-like launcher is considered in which the
51 Vulcain 2 nozzle is substituted by a dual-bell nozzle with a constant pres-
52 sure extension. This study is made in analogy with [26] where the impact of
53 the dual-bell nozzle on the payload mass delivered into a reference geosyn-
54 chronous transfer orbit (GTO) by Ariane 5 ECA was evaluated. Stark et
55 al. [26] investigated several dual-bell nozzle contours with constant pressure
56 extension by changing the area ratio of the first bell (ϵ_1) and the inflection
57 angle (α). The best solution was identified using both an analytical approach
58 based on the ideal rocket velocity increment and a trajectory optimisation
59 procedure. They showed that a significant payload gain can be obtained. In
60 the present work the goal is still to find the dual-bell geometry that max-
61 imise the payload mass inserted into a reference GTO launching from CGS
62 (Kourou), but a controlled dual-bell mode transition is assumed. The consid-
63 ered dual-bell nozzle is characterised by a first bell obtained by the method
64 of characteristic (truncated ideal contour nozzle) followed by a constant pres-
65 sure extension. Two free parameters are considered to define the dual-bell
66 nozzle geometry: the inflection angle (α) and the truncation percentage (λ)
67 of the second bell. The reference contour for the second bell is a constant
68 pressure contour ending when it reaches the direction of nozzle axis. The
69 actual bell is obtained by truncating the second bell contour to a certain

70 fraction (λ) with respect to the reference one. The design parameters are
 71 highlighted in Figure 1 where the axial x and radial r coordinates are nor-
 72 malised with respect to the throat radius R_t . It is worth noting that the area
 73 ratio of the first bell is kept fixed ($\epsilon_1 = 50$) according to the best configura-
 74 tion reported in [26], whereas the introduction of the truncation percentage
 75 (λ) of the second bell allows for beneficial nozzle weight reduction.

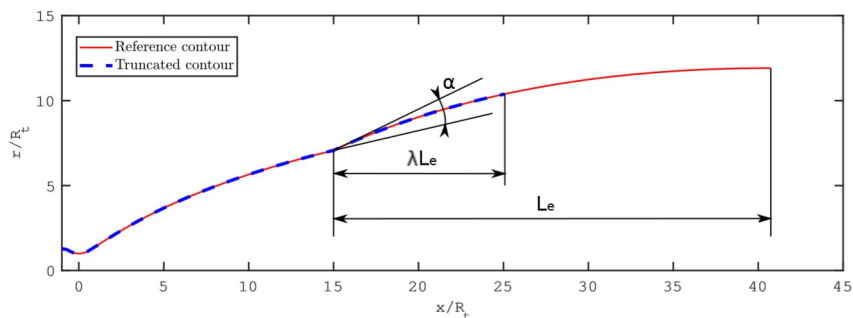


Figure 1: Dual bell nozzle with design parameters α and λ .

76 The design parameters are investigated in the intervals $7^\circ < \alpha < 17^\circ$
 77 and $0.5 < \lambda < 1$, but two size constraints are imposed on the engine length
 78 ($L_j 4.5$ m) and maximum expansion ratio ($\epsilon_2 < 150$). These values are in line
 79 with the limitations chosen by [26] which are determined by the launch pad
 80 margins. For each nozzle geometry, the ascent trajectory is optimised using
 81 a fast and efficient in-house solver based on the optimal control theory [27],
 82 similarly to previous related works [14, 15].

83 2.1. Trajectory optimisation

84 The trajectory optimization approach is briefly described in the following.
 85 Further details can be found in [14]. A point mass rocket is considered
 86 and the state equations provide the derivative of position \mathbf{r} , velocity \mathbf{v} and
 87 rocket mass m . The vectorial form of equations of motion, written in non-
 88 dimensional form to improve the integration's numerical accuracy, are

$$\frac{d\mathbf{r}}{dt} = \mathbf{v} \quad \frac{d\mathbf{v}}{dt} = \mathbf{g} + \frac{\mathbf{F} - \mathbf{D}}{m} \quad \frac{dm}{dt} = -\frac{|\mathbf{F}|}{c^* C_F} \quad (1)$$

89 where \mathbf{F} , \mathbf{D} , \mathbf{g} , c^* and C_F represent thrust, aerodynamic drag, gravity accel-
 90 eration, characteristic velocity and thrust coefficient, respectively.

Table 1: Reference launch vehicle [14].

Stage	m_p tons	F_{vac} kN	m_s tons	$I_{sp,vacm}$ s	t_b s	A_e m ²
Booster (each of 2)	480.40	-	80.60	274.0	129 ^(*)	15.38
Core Engine	-	1359	16.00	429.0	532 ^(*)	3.42
Upper stage	-	14.54	3.42	445.5	945	0.81
Fairing	-	-	3.03	-	-	-

(*) = time from lift off

Table 2: Reference mission.

Apogee (km)	Perigee (km)	Inclination (deg)	Periaxis arg. (deg)	Ref.
35943	250	6.0	178.0	[28]

91 A launcher with characteristics similar to those of the European Ariane
 92 5 ECA[29] is considered. Table 1 presents the main characteristics of the
 93 primary propulsion systems: propellant mass m_p , vacuum thrust F_{vac} , struc-
 94 tural mass m_s , vacuum specific impulse $I_{sp,vacm}$, burning time t_b and nozzle
 95 exit area A_e . The payload inserted into a reference GTO orbit (apogee
 96 altitude 35943 km, perigee altitude 250 km, inclination 6.0 deg, periaxis ar-
 97 gument 178.0 deg) is maximized for each given dual-bell geometry. Since
 98 all the other masses are kept constant, the lift-off mass is dependent on the
 99 payload. The trajectory is split into the phases outlined in Table 3.

100 The theory of optimal control[30, 31] is applied to optimize the trajectory.
 101 The Hamiltonian is defined as

$$H = \boldsymbol{\lambda}_r \mathbf{v} + \boldsymbol{\lambda}_v \left(\frac{\mathbf{r}}{|\mathbf{r}|^3} + \frac{\mathbf{F} - \mathbf{D}}{m} \right) - \lambda_m \frac{F}{c} \quad (2)$$

102 The optimal control theory provides the Euler-Lagrange equations for the
 103 adjoint variables λ_r , λ_v and λ_m

$$\frac{d\boldsymbol{\lambda}_r}{dt} = -\frac{dH}{d\mathbf{r}} \quad \frac{d\boldsymbol{\lambda}_v}{dt} = -\frac{dH}{d\mathbf{v}} \quad \frac{d\lambda_m}{dt} = -\frac{dH}{dm} \quad (3)$$

104 and boundary conditions for optimality at the boundaries of each phase, here
 105 omitted for the sake of conciseness [31]. The resulting multipoint boundary
 106 value problem, is solved by a procedure[27] based on Newton's method.

Table 3: Ascent phases.

N.	Phase	Type
1	vertical ascent to clear launch pad	fixed length 73 m, about 5 s
2	rotation phase	optimal thrust direction and duration
3	ascent with booster	zero-lift gravity-turn, ends at SRM burnout
4	main engine only with fairing	zero-lift gravity-turn, fixed time 45 s
5	main engine only with fairing	optimal thrust direction, ends when heat flux is 1135 W/m^2
6	main engine only w/o fairing	optimal thrust direction, ends at propellant depletion
7	coast arc	fixed time for staging, 10 s
8	upper-stage burn	optimal thrust direction, ends at propellant depletion
9	coast arc	ends at GTO apogee

107 The lift-off, here assumed as time reference, occurs about 7 seconds after
108 core engine ignition. Separation of boosters occurs at the reference time
109 H1 (129 s). The fairing is jettisoned during the core engine flight phase
110 as soon as aero-thermodynamic flux levels are below 1135 W/m^2 (reference
111 time FJ). After main-stage cutoff and separation, the upper stage ignition
112 occurs (reference time H2). The indirect trajectory optimization maximizes
113 the payload, i.e., the mass at upper stage cutoff (reference time H3) .

114 2.2. Dual-bell assumptions and results

115 The nozzle mass is estimated by assuming a uniform weight distribution
116 (35 kg/m^2) evaluated from the data reported by [26]. The thrust contribution
117 of the base is evaluated by performing an inviscid CFD simulation. The
118 aspiration drag in the low altitude working condition is assumed as negligible,
119 while the thrust contribution provided by the extension in the high-altitude
120 working mode is easily computed by considering a Prandtl-Meyer expansion
121 centred at the inflection point.

122 The simulations are performed assuming that the secondary injection is
123 activated (NPR_{ON}) when the natural transitional NPR is reached. The
124 natural transitional NPR is estimated by means of the Schmucker criterion
125 [32] in this preliminary evaluation. The secondary injection is deactivated
126 (NPR_{OFF}) when the launcher reaches the optimal transitional NPR which
127 guarantees the best performance of the dual-bell nozzle. The optimal NPR is
128 determined by the condition in which the dual-bell provides the same thrust
129 in both working modes.

130

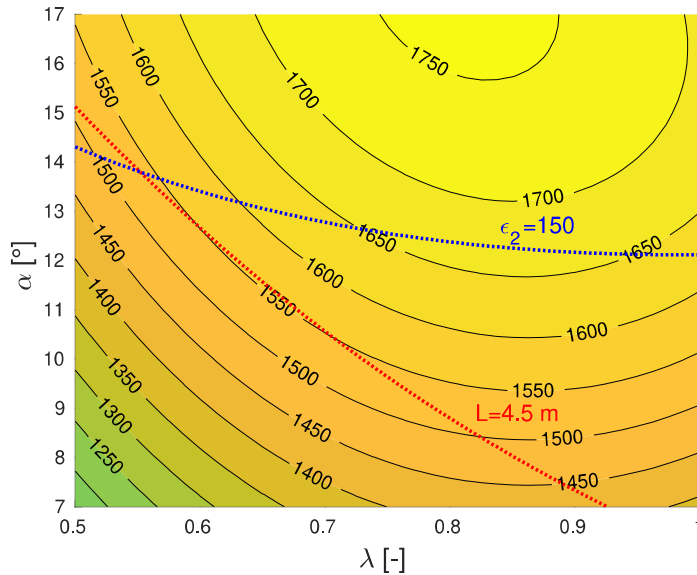


Figure 2: Optimisation results: payload gain (kg) as a function of design parameters. Red and blue dotted curves represents nozzle length constraint ($L < 4.5$ m) and maximum expansion ratio constraint ($\epsilon_2 < 150$) respectively

131 The mass flow rate \dot{m}_i used for the fluidic control is preliminary assumed
 132 to be 3 % of the main combustion chamber mass flow \dot{m} . A mass budget of
 133 $m_{CS} = 500$ kg is allocated for the fluidic control system, including both dry
 134 masses and the control fluid mass which is reduced in time according to the
 135 prescribed injection mass flow rate. The results of this preliminary paramet-
 136 ric study are reported in Figure 2 which shows the payload gain as a function
 137 of the design parameters α and λ . The plot also shows the constraint limits:
 138 feasible solutions are localised below both curves. To accurately determine
 139 the constrained optimal point, an optimisation procedure is implemented in
 140 Matlab by using the active-set algorithm for constrained optimisation [33].
 141 The optimal solution is characterised by the parameters reported in Table 4.
 142 The optimisation shows that a significant payload gain ($\Delta m_{PL} = 1556$ kg) is
 143 obtained with respect to the baseline configuration. It is worth noting that
 144 the control system is activated for a short time during which the launcher
 145 climbs from $h_{ON} = 5$ km to $h_{OFF} = 13$ km: the required control fluid mass
 146 is 230 kg.

Table 4: Preliminary optimal solution assuming $\dot{m}_i/\dot{m} = 0.03$ and $m_{CS} = 500$ kg

α [°]	11.46
λ [-]	0.6552
h_{ON} [km]	5
h_{OFF} [km]	13
NPR_{ON} [-]	222
NPR_{OFF} [-]	775
Δm_{PL} [kg]	1556

147 3. Fluidic control of transition

148 The flow field inside the optimal dual-bell nozzle is numerically studied
 149 to determine the required properties of the secondary injection at optimal
 150 NPR. Specifically, the mass flow needed to control the transition, the value of
 151 the natural transitional NPR (which determines NPR_{ON}) and the maximum
 152 NPR that can be obtained using the fluidic control (i.e maximum allowable
 153 NPR_{OFF}), are searched for. A preliminary parametric study showed that
 154 it is not possible to increase the transitional NPR up to the optimal value
 155 (NPR=775) [34]. However, the impact of the transitional NPR on the fi-
 156 nal payload is relatively small because the transition takes place when the
 157 boosters are still active. This fact suggests the choice of an alternative so-
 158 lution in which the secondary injection is used to significantly increase the
 159 transitional NPR even if the optimal transitional NPR is not reached: the
 160 goal is to minimise the occurrence of side loads by keeping the separation
 161 line fixed at the inflection point (where the magnitude of the wall pressure
 162 gradient is very large) and then letting transition take place by deactivating
 163 the secondary injection.

164 The simulations are carried out by numerically solving the Reynolds-
 165 averaged Navier-Stokes (RANS) equations based on an adaptive version of
 166 the Spalart and Allmaras model [35], which applies a compressibility correc-
 167 tion [36] only in the shear layer and has no effect on the production term in
 168 the boundary layer [21]. The flow is assumed to be 2-D axisymmetric, steady,
 169 and compressible. An ideal gas with a constant specific heat ratio $\gamma = 1.14$
 170 is considered. Viscosity is evaluated by using the Sutherland’s law for wa-
 171 ter which is the main combustion product. The nozzle wall is considered
 172 adiabatic. A parallel implicit code based on an unstructured finite-volume
 173 discretization of the domain was adopted to integrate the governing equations

174 [21]. The mesh contains 178607 cells and it is refined in the inflection region.
 175 The resolution was chosen by a grid convergence analysis performed for a
 176 previous study [34]. A plot of the dimensionless wall distance y^+ is reported
 177 in Figure 4. A second order accurate spatial discretisation is adopted and
 178 the reconstruction required by convective fluxes is limited using the Barth-
 179 Jespersen technique [37], whereas the gradient required by diffusive fluxes
 180 and source terms is computed using the weighted least square method. Con-
 181 vective fluxes are evaluated using a hybrid solver [38] that combines Flux
 182 Difference Splitting [39, 40] and the local Lax-Friedrichs (or Rusanov) flux
 183 [41]. The computational domain is discretized using the Frontal-Delaunay for
 184 quads algorithm by the Gmsh tool [42]. The unstructured grid is managed
 185 in the parallel MPI environment via the DMPlex class [43] provided by the
 186 PETSc library [44].

187

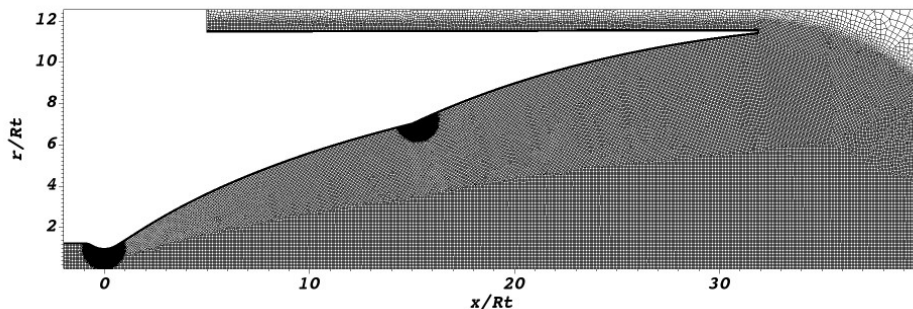


Figure 3: Detail on the mesh in the region inside the nozzle.

188 The flow field is investigated first without introducing the secondary in-
 189 jection. The Mach number contour lines at $NPR=115$ and $NPR=185$ are
 190 reported in Figure 5 which shows the low-altitude and the high-altitude work-
 191 ing modes. The wall pressure p_w distribution normalised with respect to the
 192 chamber pressure p_c is reported in Figure 6: the plot shows that the RANS
 193 simulations predict the natural transition in the range $170 < NPR < 175$.

194 However, it is possible to observe a significant displacement of the separa-
 195 tion line within the inflection region [10] when the NPR is increased from
 196 $NPR=115$ to $NPR=170$. In particular, the magnitude of the wall pressure
 197 gradient at the separation location can assume relatively small values when

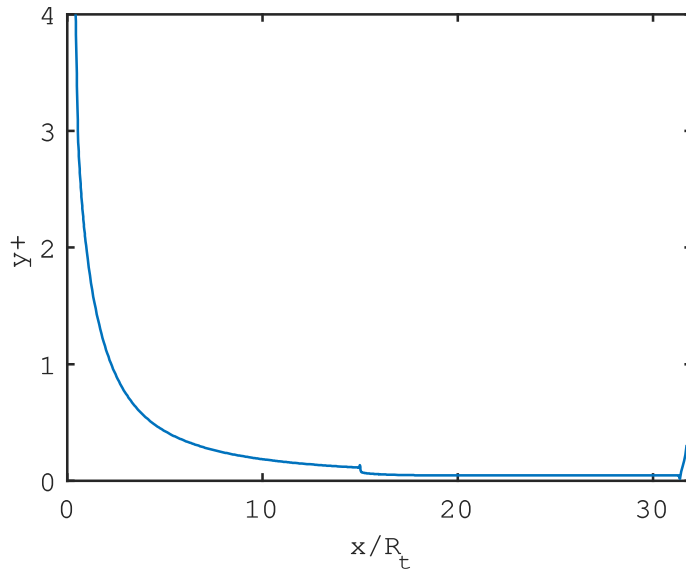


Figure 4: Dimensionless wall distance (y^+) in full flow working condition (NPR=200 without control).

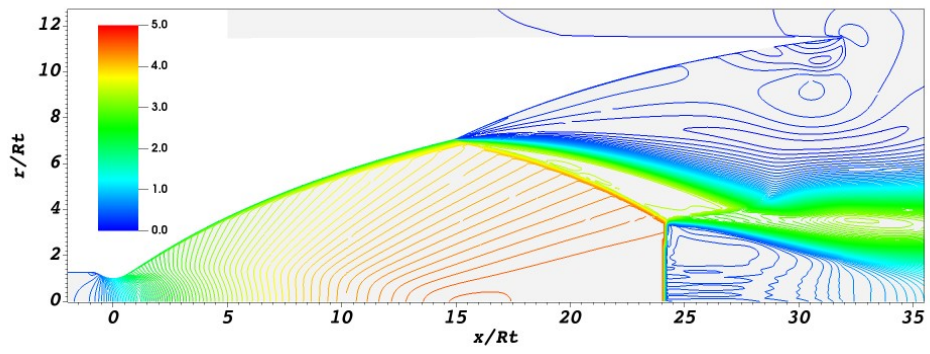
198 the NPRs increases from the sea-level condition to the transitional NPR.
 199 According to [32], the magnitude of the side loads increases when the magni-
 200 tude of the wall pressure gradient upstream of the separation point decreases:
 201 this means that significant side loads could be obtained if natural transition
 202 occurs [17]. In particular, the magnitude of the nondimensional side loads Φ
 203 can be estimated according to [32] as:

204

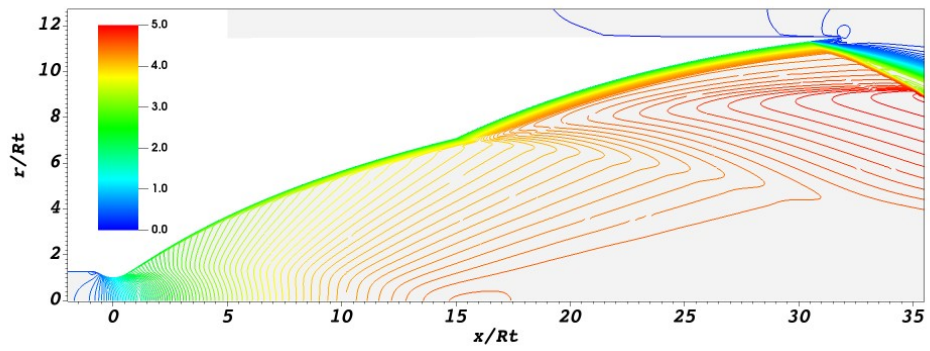
$$\Phi = \frac{F_{sl}}{2k_g k_{sl} R_t^2 p_a} = \frac{r_s p_s}{R_T p_c} \left(1 - \frac{p_s}{p_a}\right) \frac{1}{\frac{dp_s/p_c}{d(l/R_t)}} \frac{1}{1 - \frac{1 + \frac{\gamma-1}{2} M_s^2}{(1.88M_s-1)M_i} \frac{1.2}{\gamma}} \quad (4)$$

205 where F_{sl} , r_s , p_s , $\frac{dp_s/p_c}{d(l/R_t)}$ and M_s represent side loads magnitude, radius, wall
 206 pressure, normalized wall pressure gradient magnitude and wall isentropic
 207 Mach number at the separation point, respectively. The values of the constants
 208 k_g and k_{sl} are provided by [32]. However, the values of these constants
 209 are not considered here since the goal of the present work is to evaluate the
 210 nondimensional side loads in order to compare the uncontrolled and the con-
 211 trolled configurations.

212 A second set of simulations is performed by activating the secondary injection



(a)



(b)

Figure 5: Mach number contour lines at NPR=115 (a) and NPR=185 (b) without control.

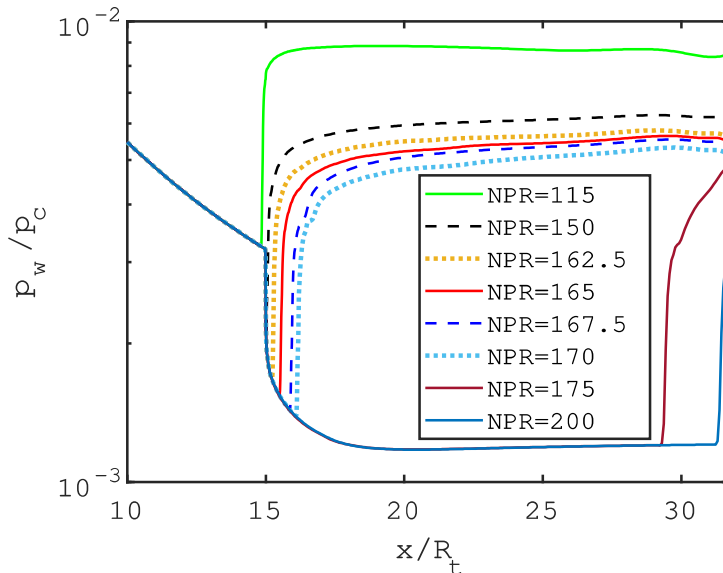
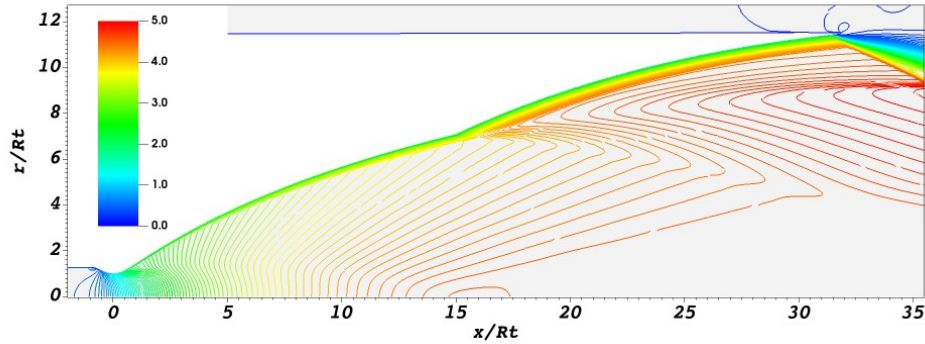


Figure 6: Wall pressure distribution in the optimized dual-bell nozzle for $115 < NPR < 175$ without control.

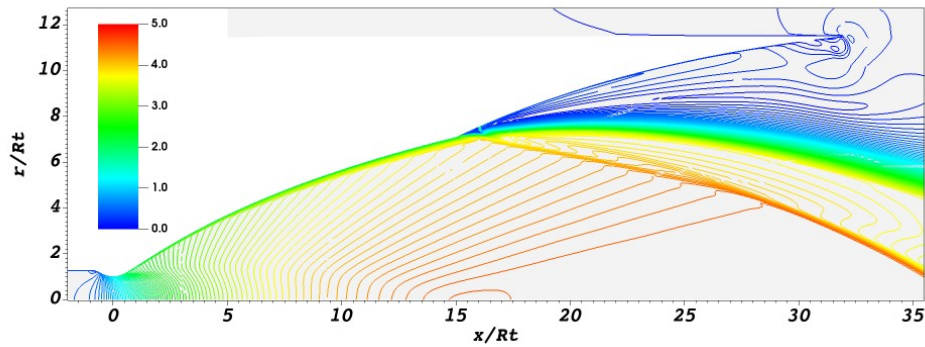
213 to delay the transition. The secondary flow is radially injected at $x/R_t = 16$
 214 through an annular slot (width equal to $0.073R_t$). The total temperature
 215 and total pressure of the injection are assumed to be equal to 300 K and
 216 1.96 bar, respectively. The flow through the injection slot is assumed to be
 217 supersonic ($M_i = 2$). A discussion on the use of sonic or supersonic injection
 218 is reported in [34]. The effect induced by the secondary injection is evident
 219 in Figure 7 which shows the Mach number contour lines at $NPR=200$ for
 220 the uncontrolled and controlled configurations: the uncontrolled flow is reat-
 221 tached while the flow with the secondary injection is still separated. The
 222 plot shows that the secondary jet acts as an obstacle for the supersonic flow,
 223 inducing a fluidic ramp and keeping the separation fixed at the inflection
 224 point. A details of the Mach number contour lines in the region around the
 225 injection slot is reported in Figure 8.

226

227 More details can be deduced from the wall pressure distribution which
 228 is reported in Figure 9 for several values of NPR: the plot shows that the
 229 separation line remains confined close to the inflection point for $NPR < 205$.
 230 This represents a significant extension of the transitional NPR with respect



(a)



(b)

Figure 7: Mach number contour lines at $NPR=200$ without control (a) and with control (b).

231 to the result obtained for the uncontrolled flow ($NPR < 175$). The effects
 232 of the secondary injection on the location of the separation line for several
 233 values of NPR is reported in Figure 10. Finally, the magnitude of the wall
 234 pressure gradient upstream of the separation line is systematically larger in
 235 the controlled flow with respect to the values observed for the natural transi-
 236 tion. This means that in the controlled flow the magnitude of the side loads
 237 is expected to be reduced with respect to the uncontrolled configuration,
 238 according to Eq. 4. This is confirmed by the plot reported in Figure 11.

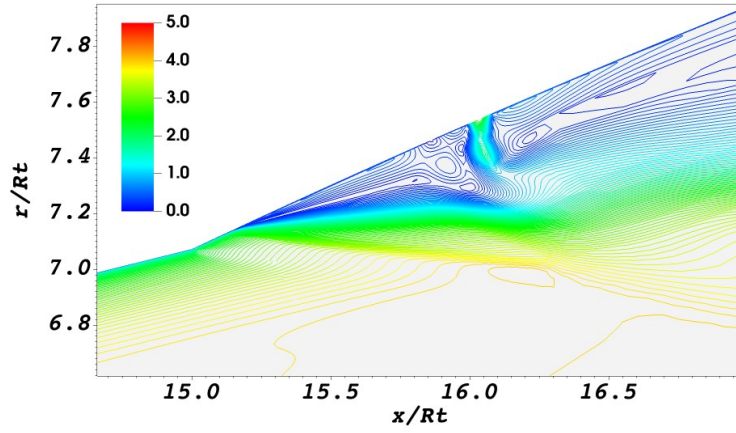


Figure 8: Mach number contour lines for the region near the injection slot at NPR=200.

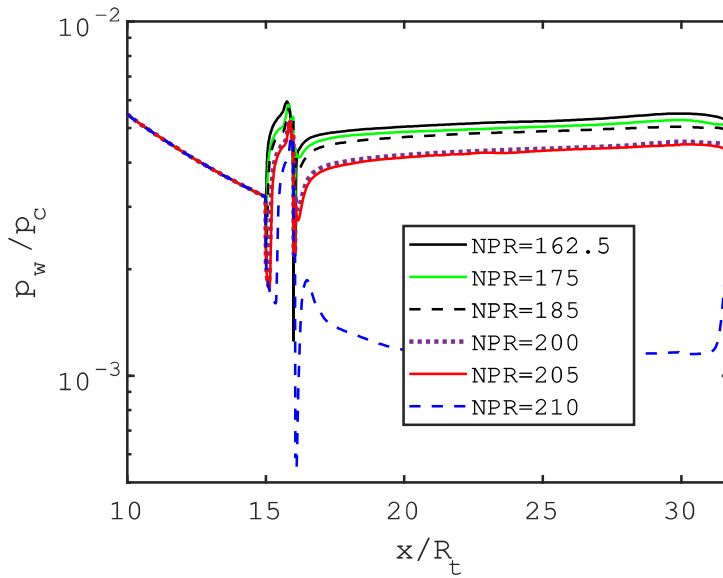


Figure 9: Wall pressure distribution in the optimized dual-bell nozzle for $175 < NPR < 220$ with secondary injection.

239 4. Corrections to the optimal solution

240 The CFD study enabled a more complete understanding of the control
 241 system requirements. In particular, the side loads estimation reported in

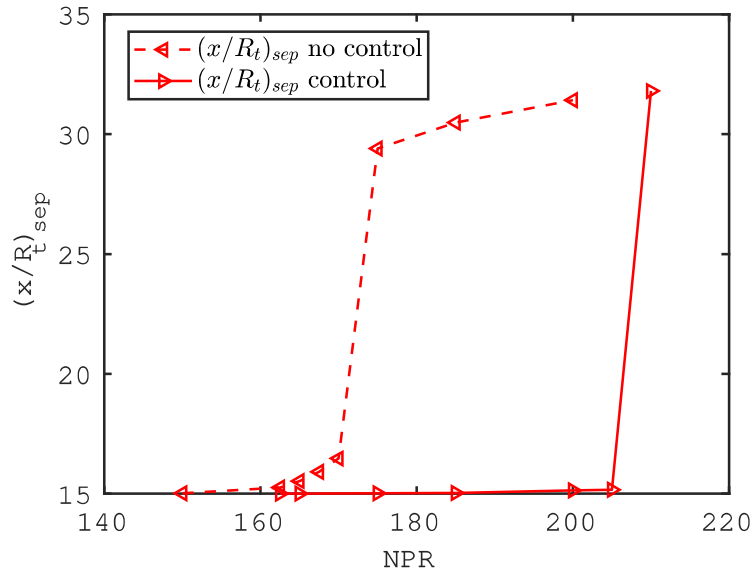


Figure 10: Separation location for uncontrolled and controlled flow.

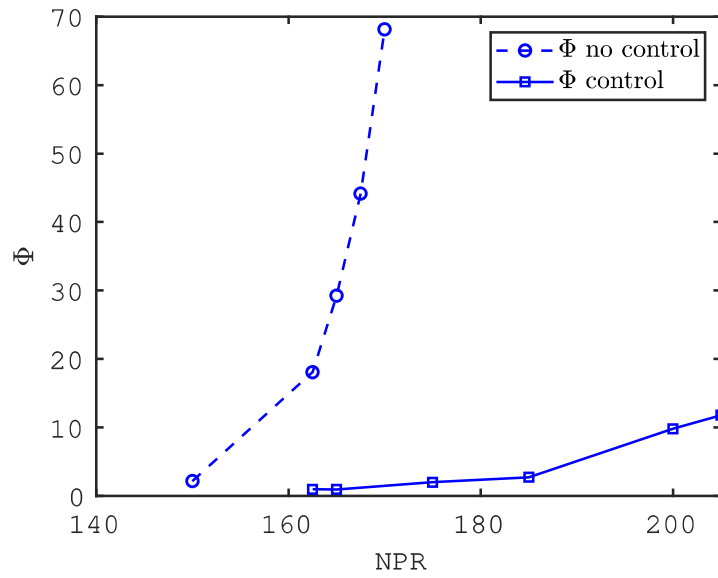


Figure 11: Nondimensional side loads for uncontrolled and controlled flow.

242 Figure 11 suggests the following choice: $NPR_{ON} = 160$ and $NPR_{OFF} = 200$.
243 In this manner, the control system is activated before significant side loads
244 are observed, and it is deactivated at a NPR significantly higher than the
245 natural transitional NPR, resulting in a rapid transition to full flow working
246 conditions.

247 The new NPR_{ON} , NPR_{OFF} and $\dot{m}_i = 0.0315\dot{m}$ are then used to run an
248 updated trajectory optimisation analysis. A first optimal configuration is
249 obtained by setting $m_{CS} = 500$ kg. Even if NPR_{OFF} was decreased from
250 the optimal value (775) to a significantly lower but feasible value (200) the
251 payload gain remains high ($\Delta m_{PL} = 1457$ kg). In this new configuration,
252 the fluidic control system remains active for approximately 10 seconds when
253 the launcher increases its altitude from 2 km to 4 km. The mass of the
254 fluid injected in this time interval is relatively small (70 kg), especially if
255 compared to the mass injected in the optimal configuration obtained by the
256 preliminary study (230 kg). For this reason, a further trajectory optimisation
257 was performed by reducing the mass budget allocated for the fluidic control
258 system to $m_{CS}=400$ kg. This has a positive effect on the payload, which is
259 increased further ($\Delta m_{PL} = 1497$ kg). In particular, the payload sensitivity
260 with respect to the additional engine mass $\frac{\partial \Delta m_{PL}}{\partial m_{CS}} \approx 0.4$ is in line with the
261 value (0.35) obtained by Stark et al.[26] through an analytical approach.
262 Finally, in Figure 12 a plot of the altitude h as a function of time is reported
263 and the key points of the mission are highlighted.

264 5. Conclusions

265 The benefits related to the use of the dual-bell nozzle in the core engine
266 of the Ariane 5-like launcher are investigated by means of a parametric study
267 in which both the nozzle geometry and the ascent trajectory were optimised.
268 There are two main results in the present work. First of all, the study showed
269 that significant payload gains can be obtained (approximately 1.5 ton in GTO
270 for an Ariane-5 like launcher). The second result is related to the effectiveness
271 of a secondary injection in controlling the separation position during the
272 ascent: this is important because side loads can be a critical issue in the real
273 application of a dual-bell. In particular, the simulations highlighted once
274 more that, in the uncontrolled flow, the separation line moves in the inflection
275 region where it is known that significant side loads can be generated. The use
276 of a secondary injection performed downstream of the inflection point consent
277 to significantly limit the displacement of the separation line, which remains

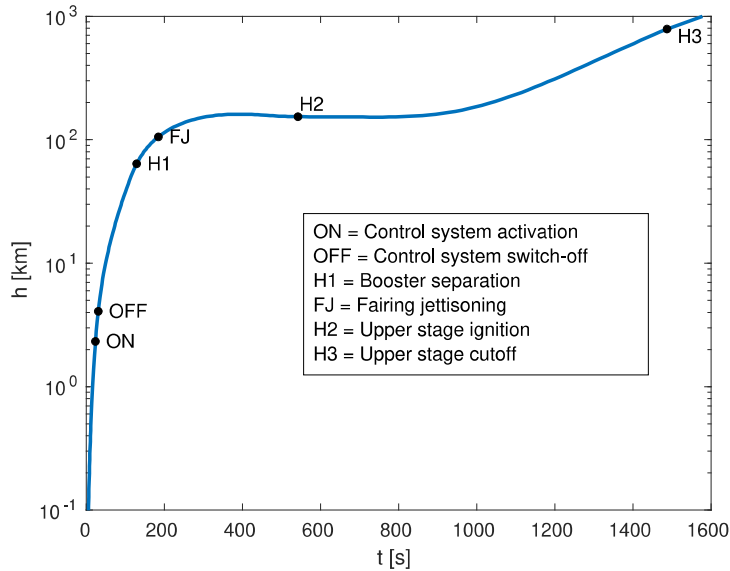


Figure 12: Optimal trajectory with controlled transition.

278 in regions characterised by a large wall pressure gradient magnitude until the
 279 injection is deactivated. This feature could be very useful to synchronise the
 280 transition in a full-liquid configuration with multiple dual-bell nozzles. The
 281 CFD simulations and the reduced activation time suggested that the control
 282 could be realised by the injection of a cold gas stored inside a dedicated tank.
 283 Alternative sources for the injected fluid will be investigated in the future, as
 284 well as, the effectiveness of fluidic control in the presence of reacting flows.

285 References

- 286 [1] G. Hagemann, H. Immich, T. Van Nguyen, G. E. Dumnov, Advanced
 287 rocket nozzles, *Journal of Propulsion and Power* 14 (5) (1998) 620–634.
- 288 [2] G. Luke, D. Adams, Use of nozzle trip rings to reduce nozzle separation
 289 side force during staging, in: *28th Joint Propulsion Conference and
 290 Exhibit*, 1992, p. 3617.
- 291 [3] N. Goncharov, V. Orlov, V. Rachuk, A. Shostak, R. Starke, Reusable
 292 launch vehicle propulsion based on the rd-0120 engine, in: *31st Joint
 293 Propulsion Conference and Exhibit*, 1995, p. 3003.

- 294 [4] V. V. Semenov, A. A. Sergienko, Rocket engine laval nozzle with gas
295 injection device (October 2008).
296 URL <https://patents.google.com/patent/W02008129372A3>
- 297 [5] R. A. Wasko, Performance of annular plug and expansion-deflection noz-
298 zles including external flow effects at transonic mach numbers, NASA-
299 TN-D-4462 (April 1968).
- 300 [6] M. Horn, S. Fisher, Dual-bell altitude compensating nozzles, Tech. rep.,
301 Rockwell International Corp., Canoga Park, CA, United States (1993).
- 302 [7] H. Immich, M. Caporicci, Festip technology developments in liquid
303 rocket propulsion for reusable launch vehicles, in: 32nd Joint Propulsion
304 Conference and Exhibit, 1997, p. 3113.
- 305 [8] M. Frey, G. Hagemann, Critical assessment of dual-bell nozzles, *Journal*
306 *of propulsion and power* 15 (1) (1999) 137–143.
- 307 [9] F. Nasuti, M. Onofri, Theoretical analysis and engineering modeling of
308 flowfields in clustered module plug nozzles, *Journal of Propulsion and*
309 *Power* 15 (4) (1999) 544–551.
- 310 [10] F. Nasuti, M. Onofri, E. Martelli, Role of wall shape on the transition in
311 axisymmetric dual-bell nozzles, *Journal of propulsion and power* 21 (2)
312 (2005) 243–250.
- 313 [11] E. Martelli, F. Nasuti, M. Onofri, Numerical parametric analysis of dual-
314 bell nozzle flows, *AIAA journal* 45 (3) (2007) 640–650.
- 315 [12] R. Parsley, K. van Stelle, Altitude compensating nozzle evaluation, in:
316 28th Joint Propulsion Conference and Exhibit, 1992, p. 3456.
- 317 [13] L. Boccaletto, J.-P. Dussauge, High-performance rocket nozzle concept,
318 *Journal of Propulsion and Power* 26 (5) (2010) 969–979.
- 319 [14] L. Casalino, D. Pastrone, F. Simeoni, Effects of limitation of nozzle flow
320 separation on launcher performance, *Journal of Propulsion and Power*
321 29 (4) (2013) 849–854. doi:10.2514/1.B34669.
- 322 [15] A. Ferrero, D. Pastrone, Plasma actuator–assisted rocket nozzle for im-
323 proved launcher performance, *AIAA Journal* 57 (4) (2019) 1348–1354.

- 324 [16] I. Ivanov, I. Kryukov, Numerical study of ways to prevent side loads in
325 an over-expanded rocket nozzles during the launch stage, *Acta Astro-*
326 *nautica* 163 (2019) 196–201.
- 327 [17] C. Genin, R. H. Stark, Side loads in subscale dual bell nozzles, *Journal*
328 *of Propulsion and Power* 27 (4) (2011) 828–837.
- 329 [18] M. Cimini, E. Martelli, M. Bernardini, Numerical analysis of side-loads
330 reduction in a sub-scale dual-bell rocket nozzle, *Flow, Turbulence and*
331 *Combustion* (2021) 1–24.
- 332 [19] T. Tomita, M. Takahashi, M. Sasaki, Control of transition between
333 two working modes of a dual-bell nozzle by gas injection, in: 45th
334 AIAA/ASME/SAE/ASEE Joint Propulsion Conference & Exhibit,
335 2009, p. 4952.
- 336 [20] V. Zmijanovic, L. Leger, M. Sellam, A. Chpoun, Assessment of transi-
337 tion regimes in a dual-bell nozzle and possibility of active fluidic control,
338 *Aerospace Science and Technology* 82 (2018) 1–8.
- 339 [21] A. Ferrero, E. Martelli, F. Nasuti, D. Pastrone, Fluidic control of transi-
340 tion in a dual-bell nozzle, in: *AIAA Propulsion and Energy 2020 Forum*,
341 2020, p. 3788.
- 342 [22] E. Martelli, F. Nasuti, M. Onofri, Film cooling effect on dual-bell nozzle
343 flow transition, in: 45th AIAA/ASME/SAE/ASEE Joint Propulsion
344 Conference & Exhibit, 2009, p. 4953.
- 345 [23] D. Proschanka, K. Yonezawa, H. Koga, Y. Tsujimoto, T. Kimura,
346 K. Yokota, Control of operation mode transition in dual-bell nozzles
347 with film cooling, *Journal of Propulsion and Power* 28 (3) (2012) 517–
348 529.
- 349 [24] R. Stark, C. Génin, C. Mader, D. Maier, D. Schneider, M. Wohlhüter,
350 Design of a film cooled dual-bell nozzle, *Acta Astronautica* 158 (2019)
351 342–350.
- 352 [25] D. Schneider, R. Stark, C. Génin, M. Oswald, K. Kostyrkin, Active
353 control of dual-bell nozzle operation mode transition by film cooling and
354 mixture ratio variation, *Journal of Propulsion and Power* 36 (1) (2020)
355 47–58.

- 356 [26] R. Stark, C. Génin, D. Schneider, C. Fromm, Ariane 5 performance
357 optimization using dual-bell nozzle extension, *Journal of Spacecraft and*
358 *Rockets* 53 (4) (2016) 743–750.
- 359 [27] G. Colasurdo, D. Pastrone, Indirect optimization method for im-
360 pulsive transfers, in: *Astrodynamics Conference*, 1994, p. 3762.
361 doi:10.2514/6.1994-3762.
- 362 [28] Ariane 5 User’s Manual, Arianespace, Evry-Courcouronnes, France,
363 2008.
- 364 [29] S. Isakowitz, J. Hopkins, J. Hopkins Jr, *International Reference Guide*
365 *to Space Launch Systems*, American Institute of Aeronautics and As-
366 tronautics, Inc., 1994.
- 367 [30] A. E. Bryson, Y.-C. Ho, *Applied optimal control*, Hemisphere Publishing
368 Co., 1975.
- 369 [31] L. Casalino, G. Colasurdo, D. Pastrone, Optimal low-thrust escape tra-
370 jectories using gravity assist, *Journal of Guidance, Control, and Dynam-*
371 *ics* 22 (5) (1999) 637–642.
- 372 [32] R. H. Schmucker, Flow process in overexpanded chemical rocket nozzles.
373 part 1: Flow separation, NASA TM-77396 (January 1984).
- 374 [33] P. E. Gill, W. Murray, M. H. Wright, *Practical optimization*, SIAM,
375 2019.
- 376 [34] A. Ferrero, A. Conte, E. Martelli, F. Nasuti, D. Pastrone, Dual-bell
377 nozzle for space launchers with fluidic control of transition, in: *AIAA*
378 *Propulsion and Energy 2021 Forum*, 2021, p. 3586.
- 379 [35] S. R. Allmaras, F. T. Johnson, Modifications and clarifications for the
380 implementation of the spalart-allmaras turbulence model, in: *Seventh*
381 *international conference on computational fluid dynamics (ICCFD7)*,
382 2012, pp. 1–11.
- 383 [36] R. Paciorri, F. Sabetta, Compressibility correction for the spalart-
384 allmaras model in free-shear flows, *Journal of Spacecraft and Rockets*
385 40 (3) (2003) 326–331.

- 386 [37] T. Barth, D. Jespersen, The design and application of upwind schemes
387 on unstructured meshes, in: 27th Aerospace sciences meeting, 1989, p.
388 366.
- 389 [38] A. Ferrero, D. D'Ambrosio, A hybrid numerical flux for supersonic flows
390 with application to rocket nozzles, *Advances in Aircraft and Spacecraft*
391 *Science* 7 (5) (2020) 387–404.
- 392 [39] S. Osher, F. Solomon, Upwind difference schemes for hyperbolic systems
393 of conservation laws, *Mathematics of computation* 38 (158) (1982) 339–
394 374.
- 395 [40] M. Pandolfi, A contribution to the numerical prediction of unsteady
396 flows, *AIAA journal* 22 (5) (1984) 602–610.
- 397 [41] V. V. Rusanov, The calculation of the interaction of non-stationary
398 shock waves and obstacles, *USSR Computational Mathematics and*
399 *Mathematical Physics* 1 (2) (1962) 304–320.
- 400 [42] C. Geuzaine, J.-F. Remacle, Gmsh: A 3-d finite element mesh generator
401 with built-in pre-and post-processing facilities, *International journal for*
402 *numerical methods in engineering* 79 (11) (2009) 1309–1331.
- 403 [43] M. Lange, M. G. Knepley, G. J. Gorman, Flexible, scalable mesh and
404 data management using petsc dmpex, in: *Proceedings of the 3rd Inter-*
405 *national Conference on Exascale Applications and Software*, University
406 of Edinburgh, 2015, pp. 71–76.
- 407 [44] S. Balay, S. Abhyankar, M. Adams, J. Brown, P. Brune, K. Buschelman,
408 L. Dalcin, A. Dener, V. Eijkhout, W. Gropp, et al., *Petsc users manual*
409 (2019).